Comparison of modeling methods and parametric study for a piezoelectric wind energy harvester

Zhao, Liya; Tang, Lihua; Yang, Yaowen

2013

Comparison of Modeling Methods and Parametric Study for Piezoelectric Wind Energy Harvester

Liya Zhao, Lihua Tang and Yaowen Yang*

School of Civil and Environmental Engineering, Nanyang Technological University, 50 Nanyang Avenue, 639798, Singapore

*Corresponding author, Email: cywyang@ntu.edu.sg

Abstract

Harvesting flow energy by exploiting transverse galloping of a bluff body attached to a piezoelectric cantilever is a prospective method to power the wireless sensing systems. In order to better understand the electroaeroelastic behavior and further improve the galloping piezoelectric energy harvester (GPEH), an effective analytical model is required, which needs to incorporate both the electromechanical coupling and aerodynamic force. Available electromechanical models for GPEH include lumped parameter single-degree-of-freedom (SDOF) model, approximated distributed parameter model based on Rayleigh-Ritz discretization, and distributed parameter model with Euler-Bernoulli beam representation. Each modelling method has its own advantages. The corresponding aerodynamic models are formulated using quasi-steady hypothesis (QSH). In this paper, SDOF model, Euler-Bernoulli distributed parameter model using single mode and Euler-Bernoulli distributed parameter model using multi-modes are compared and validated with experimental results. Based on the comparison and validation, the most effective model is employed for the subsequent parametric study. The effects of load resistance, wind exposure area of the bluff body, mass of the bluff body and length of the piezoelectric sheets on the power output are investigated. These simulations can be exploited for designing and optimizing GPEHs for better performance.

1. Introduction

Wireless sensing systems have been widely used in structural health monitoring. Due to the inconvenience and high cost of replacement of batteries, development of self-powered sensor nodes by harvesting ambient energy has been researched explosively in the past few years. Ambient mechanical vibrations can be converted to electricity via electrostatic [1], electromagnetic [2], piezoelectric [3] and magnetostrictive [4] mechanisms, among which piezoelectric transduction has attracted much interest because of its high power density and non-reliance on external magnetic field or initial voltage. Many studies have been conducted on energy harvesting using piezoelectric materials [5-11]. These studies mainly focus on converting the preexisting structural vibrations into electricity. However, piezoelectric energy harvesting from small wind has received only limited attention.

When structures are subjected to wind flows, aeroelastic instabilities such as vortex-induced vibrations, galloping, flutter and buffeting may occur given specific conditions. The energy of such wind-induced vibrations can be beneficially converted into electricity via the piezoelectric transduction mechanism. Many studies have been conducted on harnessing wind energy by exploiting these aeroelastic instabilities [12-39].

Some researchers proposed the energy harvesters with flapping wings to convert aeroelastic flutter vibrations into electricity [12-22]. Bryant and Garcia [15] analyzed the flutter boundary and limit cycle behavior of a piezoelectric bimorph with a rigid flap connected to the tip. A peak power of 2.2mW was obtained at 7.9m/s. Erturk *et al.* [16] investigated the potential of harvesting energy from aeroelastic vibrations with a piezoaeroelastic airfoil. Linear analysis of power generation at flutter boundary was performed. Different from the use of flapping wings, several other devices with alternative structural designs were proposed to extract power from aeroelastic instabilities. Li *et al.* [23] developed a bio-inspired piezo-leaf architecture which generated electricity by cross-flow fluttering motion, gaining a peak power of 600μW. Kwon [24] experimentally investigated the power output of a T-shaped piezoelectric cantilever, and obtained the empirical formula to calculate the cut-in wind speed. Wind energy harvesters employing vortex-induced vibrations were also frequently investigated, which were usually designed as a linear mechanical resonator with a cylinder placed windward [25-29]. Maximum power output was achieved when the frequency of vortex shedding approaches the natural frequency of the harvester. Akaydin *et al.* [28] tested the efficiency of such a harvester and obtained a maximum power of 0.1mW at 1.192m/s. The main constraint of such harvesters is the narrow wind speed range for effective power generation. Jung and Lee [30] studied the performance of a harvester exploiting wake galloping with two paralleled cylinders. Electromagnetic induction was employed other than the piezoelectric transduction. Recent progress on wind energy harvesting also includes a damped cantilever pipe carrying flowing fluid proposed by Elvin and Elvin [31] and a harmonica-type aeroelastic micropower generator developed by Bibo *et al.* [32].

Translational galloping is another aeroelastic instability phenomenon giving rise to transverse oscillations normal to the wind flow direction in structures with weak damping, when the wind speed exceeds a critical value. It is a better choice to obtain structural vibrations for energy harvesting purpose compared to the vortex-induced vibrations and flutter, for its advantage of large oscillation amplitude and the ability of oscillating in infinite range of wind velocities [36,45]. Translational galloping was first analyzed by Den Hartog [40], and a criterion for galloping stability was introduced. Many researchers have studied the effect of various parameters on the galloping stability of different structures, including the angle of attack, cross-section geometries, flow turbulence, Reynolds number, etc [41-45]. Barrero-Gil *et al.* [33] theoretically analyzed the potential use of transverse galloping to harvest energy using an SDOF model. No specific design of harvester device was proposed. Abdelkefi *et al.* [34] considered a GPEH with a square prism as the bluff body, and investigated the effects of Reynolds number and load resistance on the threshold of galloping and the level of harvested power. They further theoretically compared the performances of different cross-section geometries of the bluff body for GPEHs with linear and nonlinear analysis [35]. An SDOF model was employed for these two studies, with the value of electromechanical coupling manually specified. Yang *et al.* [36] experimentally studied the influence of cross-section geometry on the performance of GPEHs, and validated the established SDOF model with the experimental results. Sirohi and Mahadik [37] studied a GPEH consisting of two piezoelectric cantilevers connected to a prism with equilateral triangular section. They also developed another GPEH using a composite piezoelectric cantilever connected in parallel to a prism with

D-shaped section [38]. For these two harvesters, an approximated distributed parameter model based on energy method (Rayleigh-Ritz type of discretization) was used. Abdelkefi *et al*. [39] employed the harvester design of Sirohi and Mahadik [37] and further studied the influence of load resistance on the threshold of galloping and harvested power level with an Euler-Bernoulli distributed parameter model. Single mode (fundamental mode) was considered in their analysis. In all the analytical models mentioned above, the aerodynamic forces were formulated based on QSH. Each model method has its own merits, such as the simple form and ease of application of the SDOF model, and the accuracy of the distributed parameter models. Although many studies have been conducted on the issues of the electromechanical models for vibration piezoelectric energy harvesters under base excitation [46, 47], more work need to done on the modeling and better designing of GPEH which incorporate the aerodynamic forces.

This article compares different modeling methods for GPEHs. SDOF model established in the preceding study [36], Euler-Bernoulli distributed parameter model using single mode and multi-modes are considered followed by experimental validation. The merits, disadvantages and applicability of these methods are discussed. Subsequently, employing the most effective model from the comparison, parametric study is performed to study the effects of load resistance, wind exposure area of the bluff body, mass of the bluff body and length of the piezoelectric sheets on the electroaeroelastic behavior (cut-in wind speed and power output level) of GPEHs. The results can be exploited for designing and optimizing GPEHs for better power output performance.

2. Mechanism of galloping
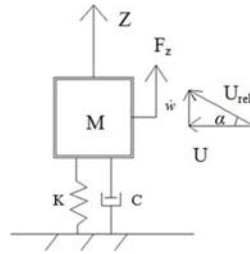
Figure 1. Schematic of a bluff body undergoing galloping

Translational galloping is a self-excited phenomenon giving rise to large amplitude oscillations of bluff body when subjected to wind flows. Assume that a bluff body is elastically mounted as shown in figure 1. The governing equation of the galloping motion can be written as

$$M\ddot{w}(t) + C\dot{w}(t) + Kw(t) = F_z(t) \tag{1}$$

where w is the vertical position of the bluff body in z direction; M is the mass of the bluff body; C is the damping coefficient; K is the stiffness of the system and F_z is the aerodynamic force. The overdot denotes differentiation with respect to time t. F_z can be expressed as [45]

$$F_z = \frac{1}{2}\rho_a S_{tip} U^2 C_{Fz} \tag{2}$$

where ρ_a is the air density; S_{tip} is the exposure area facing the flow; U is the wind speed and C_{Fz} is the total aerodynamic force coefficient in z direction. QSH is employed here, which considers that the aerodynamic force during galloping oscillation is equal to that when the bluff body is steady with the corresponding angle of attack. This hypothesis is applicable when the oscillation is slow enough, which requires that the characteristic timescale of the flow is much smaller than the characteristic timescale of the oscillation, corresponding to the character of galloping phenomenon. The larger the wind speed, the safer to use QSH. QSH has been confirmed to be able to successfully model galloping in many studies [40,41,45]. For a specific cross-section geometry, C_{Fz} is a function of the angle of attack α (figure 1), and can be determined through experiments [40-45]. It is common to express C_{Fz} as a polynomial expansion as

$$C_{Fz} = \sum_{r=1,2,...} A_r (\alpha)^r \tag{3}$$

where A_r are empirical coefficients for the polynomial fitting [33,45]. If the bluff body undergoes only translational oscillation without rotation, α can be expressed as

$$\alpha = \frac{\dot{w}}{U} \tag{4}$$

Substituting Eqs. (2-4) into Eq. (1), and dividing both sides by M yields

$$\ddot{w}(t) + \left(2\varsigma\omega_n - \frac{1}{2M} \rho_a S_{tip} U \left[\sum_{r=1,2,...} A_r (\frac{\dot{w}}{U})^{r-1} \right] \right) \dot{w} + \omega_n^2 w = 0 \tag{5}$$

where ς is the damping ratio and ω_n is the natural frequency of the system. The aerodynamic force can be considered as an effective nonlinear damping as shown in Eq.(5), rendering the galloping "self-excited". The criterion for galloping instability, which is identified by Den Hartog [40], is expressed as

$$\frac{\partial C_{Fz}}{\partial \alpha} > 0 \tag{6}$$

The criterion requires $A_1 > 0$. For arbitrarily small $\dot{w}$, the system is controlled by the linear damping $2\varsigma\omega_n - \frac{1}{2M} \rho_a S_{tip} U A_1$, which is positive, thus the oscillations will be damped to the zero equilibrium. When U increases and exceeds a certain value, the linear damping becomes negative, giving rise to galloping oscillations of the bluff body (Hopf bifurcation). When $\dot{w}$ is large enough due to the increasing oscillation amplitude, the nonlinear damping $\frac{1}{2M} \rho_a S_{tip} U \left[\sum_{r=2,...} A_r (\frac{\dot{w}}{U})^{r-1} \right]$ should be taken into account which makes the overall damping non-negative. Limit cycle oscillation will occur when the damping reaches zero. Due to the self-excited and self-limiting characteristics of galloping, it is a prospective energy source for energy harvesting.

3. Comparison of modelling methods for galloping piezoelectric energy harvester

A typical GPEH is usually designed as a piezoelectric cantilever attached with a bluff body at the free end, as shown in Figure 2. The bluff body, which is with a specific cross section, oscillates in the direction normal to the incoming flow due to galloping. Two piezoelectric sheets are bonded to each side of the substrate beam, generating electricity from the

mechanical strain which is developed due to the bluff body oscillation. The analytical model of a GPEH should consider both the electromechanical coupling effect and the aerodynamic force acting on the bluff body. Commonly used models for GPEHs include the SDOF model, approximate distributed parameter model with Rayleigh-Ritz type of discretization, and Euler-Bernoulli distributed parameter model with exact analytical mode shapes. The main difference between these models lies in the representation of the electromechanical coupling term. This section will compare the merits, disadvantages and applicabilities of the lumped parameter and distributed parameter models. The aerodynamic forces are all formulated based on quasi-steady hypothesis, although their representation formulas are various due to the different mechanical parameters employed in the corresponding electromechanical equations. The power storage technique is not considered in this paper, so the simple electric circuit only consists of an external resistive load R_L.
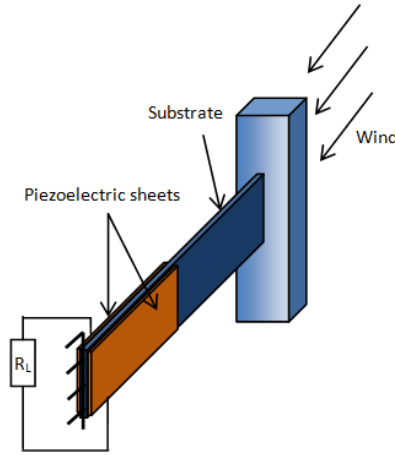
Figure 2. Schematic of a typical GPEH

3.1. SDOF model

In the preceding study, a simple SDOF model was established to simulate the electroaeroelastic behavior of a GPEH [36]. In that model, the harvester was considered to oscillate close to the fundamental frequency, which was confirmed with visual observation during the experiment. The governing equations are given as

$$\begin{cases} M_{eff}\ddot{w}(L,t)+C_{eff}\dot{w}(L,t)+K_{eff}w(L,t)+\Theta V(t)=F_z(t)=\dfrac{1}{2}\rho_a h l_{tip}U^2 C_{Fz} \\ \dfrac{V(t)}{R_L}+C_P\dot{V}(t)-\Theta\dot{w}(L,t)=0 \end{cases} \tag{7}$$

where $w(L,t)$ is the displacement of the bluff body in the direction normal to the wind flow; C_{eff} and K_{eff} are the effective damping and stiffness of the harvester; $V(t)$ is the generated voltage across ; C_P is the total capacitance of two piezoelectric sheets with parallel connection; Θ is the electromechanical coupling term; h and l_{tip} are the frontal dimension and length of the bluff body, the product of which equals to S_{tip}; and M_{eff} is the effective mass approximated as $M_{eff}=33/140M_b+M_{tip}$, where M_b and M_{tip} are the mass of the cantilever and the bluff body. Θ is determined easily though experiments by

$$\Theta = \sqrt{(\omega_{noc}{}^2 - \omega_{nsc}{}^2)M_{eff}C_P} \tag{8}$$

where ω_{noc} and ω_{nsc} are the open circuit and short circuit resonant frequencies of the harvester. C_{Fz} is expressed as in Eq. (3), and the attack angle is modified to $\alpha = \dot{w}(L,t)/U + w'(L,t)$, where $w'(L,t)$ is the rotation angle at the free end due to the deflection of the beam, approximated as $w'(L,t) = 3w(L,t)/2L$.

By defining a state vector X:

$$X = \begin{Bmatrix} X_1 \\ X_2 \\ X_3 \end{Bmatrix} = \begin{Bmatrix} w(L,t) \\ \dot{w}(L,t) \\ V(t) \end{Bmatrix} \tag{9}$$

the governing equations can be written in the state space form as

$$\dot{X} = \begin{Bmatrix} \dot{w}(L,t) \\ \ddot{w}(L,t) \\ \dot{V}(t) \end{Bmatrix} = \begin{Bmatrix} X_2 \\ -2\varsigma\omega_n X_2 - \omega_n^2 X_1 - \dfrac{\Theta}{M_{eff}} X_3 + \dfrac{\rho_a h l_{tip} U^2}{2M_{eff}} \left[\displaystyle\sum_{r=1,2,\ldots} A_r \left(\dfrac{X_2}{U} + \dfrac{3X_1}{2L} \right)^r \right] \\ \dfrac{\Theta}{C_P} X_2 - \dfrac{X_3}{R_L C_P} \end{Bmatrix} \tag{10}$$

where $2\zeta\omega_n = C_{eff}/M_{eff}$ and $\omega_n = \omega_{nsc}$. Eq. (10) can then be numerically solved in MATLAB using the solver like ode45 to determine the vibration response of the beam, cut-in wind speed, and generated voltage across R_L. The average power P_{ave} is related with the root mean square (RMS) voltage V_{RMS} as $P_{ave} = V_{RMS}^2/R_L$.
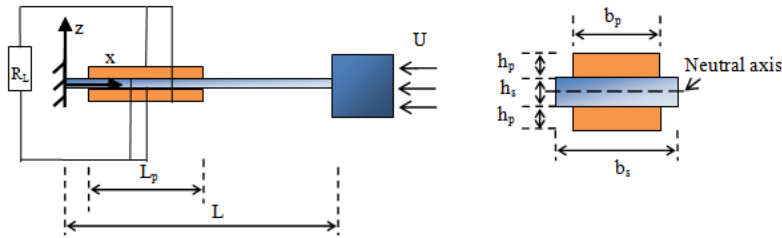
3.2. Euler-Bernoulli distributed parameter model

Figure 3. (a) Top view of the considered GPEH and (b) cross-section of the composite beam for $x_1 < x < x_2$.

Distributed parameter electromechanical models based on Euler-Bernoulli beam theory have been studied a lot for vibration piezoelectric energy harvesters with base-excitations [5,46,47]. For a GPEH, the electromechanical equations are developed based on similar assumptions: (a) The Euler-Bernoulli beam assumptions are applied to the composite beam; (b) The perfectly conductive electrodes fully cover the top and bottom surfaces of the piezoelectric sheet inducing uniform electric field through the thickness; (c) Only the z-direction vibration (transverse vibration) is considered; (d) The damping mechanisms including the internal strain rate damping and external air damping satisfy the proportional damping criterion. The schematics of the GPEH showing the coordinate directions and the cross-section of the composite beam are presented in figure 3. We consider the parallel connected situation for the two piezoelectric sheets. The coupled governing equations for the GPEH can be written as [5, 39]

$$
\begin{cases}
\dfrac{\partial^2}{\partial x^2}\left[YI(x)\dfrac{\partial^2 w(x,t)}{\partial x^2}\right] + c_s I(x)\dfrac{\partial^5 w(x,t)}{\partial x^4 \partial t} + c_a \dfrac{\partial w(x,t)}{\partial t} + m(x)\dfrac{\partial^2 w(x,t)}{\partial t^2} + \theta V(t)\left[\dfrac{d\delta(x-x_1)}{dx} - \dfrac{d\delta(x-x_2)}{dx}\right] = F_z\delta(x-L) \\[3mm]
\dfrac{V(t)}{R_L} + C_p\dfrac{dV(t)}{dt} - \theta\displaystyle\int_{x_1}^{x_2}\dfrac{\partial^3 w(x,t)}{\partial x^2 \partial t}dx = 0
\end{cases}
$$

(11)

where $w(x, t)$ is the transverse deflection of the beam in z direction; $\delta(x)$ is the Dirac delta function; c_s and c_a are the coefficients of strain rate damping and air damping; $m(x)$ is the distributed mass of the beam, being expressed as $m(x)=\rho_s h_s b_s$ for $0<x<x_1$ and $x_2<x<L$, and $m(x)=\rho_s h_s b_s+2\rho_p h_p b_p$ for $x_1<x<x_2$, where ρ_s, h_s and b_s are the mass density, thickness and width of the substrate, respectively, ρ_p, h_p and b_p are the corresponding terms of the piezoelectric sheet, and x_1 and x_2 are respectively the starting and ending positions of the piezoelectric sheets along the beam; $YI(x)$ is the bending stiffness of the composite beam expressed as $YI(x)=Y_s b_s h_s^3/12$ for $0<x<x_1$ and $x_2<x<L$, and $YI(x)=Y_s b_s h_s^3/12+2Y_p b_p[(h_p+h_s/2)^3-h_s^3/8]/3$ for $x_1<x<x_2$, where Y_s and Y_p are the Young's modulus of the substrate and piezoelectric material, respectively; θ is the piezoelectric coupling term given by $\theta=-Y_p d_{31} b_p(h_p+h_s)$, where d_{31} is the piezoelectric constant; and C_p is the total capacitance as in the SDOF model, being given by $C_p=2\varepsilon_{33}^S b_p(x_2-x_1)/h_p$ ((x_2-x_1) equals to the length of the piezoelectric sheets L_p), where ε_{33}^S is the permittivity at constant strain. As in the SDOF model, F_z is the aerodynamic force due to galloping.

The transverse deflection $w(x,t)$ can be represented as

$$
w(x,t) = \sum_{r=1}^{\infty}\phi_r(x)\eta_r(t)
$$
(12)

where $\phi_r(x)$ is the mass normalized mode shape for the rth mode of the corresponding undamped free vibration problem; and $\eta_r(t)$ is the modal coordinate. Erturk and Inman [5,46,47] presented the procedure for the exact analytical solution of $\phi_r(x)$ for the cantilever fully and uniformly covered with piezoelectric materials. As for the cantilever beam which is partially covered by piezoelectric sheets (the case for our prototype in the experiment), Abdelkefi el al. [39] developed the Euler-Bernoulli distributed parameter model by deriving the exact analytical mode shape function to analyze the electroaeroelastic behavior of a

GPEH. Yet such analytical solution for the segmented mode shapes is quite cumbersome. Single mode (fundamental mode only) was considered in their analysis. In this paper, we obtain $\phi_r(x)$ and $\phi_r{}'(x)$ easily by finite element method in Matlab. Hermite cubic functions are employed as the interpolation functions for the beam element.

F_z is still in the form as in the SDOF model (Eq. (7)), but the attack angel is here expressed in modal coordinates:

$$\alpha = \frac{\sum_{r=1}^{\infty} \phi_r(L)\eta_r(t)}{U} + \sum_{r=1}^{\infty} \phi_r{}'(L)\eta_r(t) \tag{13}$$

Subsequently, introducing Eqs. (12) and (13) into Eq. (11) yields the coupled governing equations in modal coordinates:

$$\begin{cases} \ddot{\eta}_r(t) + 2\zeta_r\omega_r\dot{\eta}_r(t) + \omega_r^2\eta_r(t) + \chi_r V(t) = \phi_r(L) \times \frac{1}{2}\rho_a h l_{tip} U^2 \sum_{i=1,2\ldots} A_i \left[\frac{\sum_{r=1}^{\infty}\phi_r(L)\dot{\eta}_r(t)}{U} + \sum_{r=1}^{\infty}\phi_r{}'(L)\eta_r(t) \right]^i \\ \frac{V(t)}{R_L} + C_p\dot{V}(t) - \sum_{r=1}^{\infty}\chi_r\dot{\eta}_r(t) = 0 \end{cases}$$

$$\tag{14}$$

where ζ_r is the modal mechanical damping; ω_r is the undamped natural frequency of the rth vibration mode; and χ_r is the modal electromechanical coupling term written as $\chi_r = \theta[\phi_r{}'(x_2) - \phi_r{}'(x_1)]$. Before proceeding to solve Eq. (14), a short explanation of how to evaluate ζ_r is presented here. As mentioned in assumption (d), the mechanical damping which includes the internal strain rate damping and external air damping is treated with the proportional damping (Rayleigh damping) assumption. For a uniform piezoelectric beam of which the flexural rigidity YI and mass per unit length m are both uniformly distributed [5,46,47], ζ_r can be simply expressed as $\zeta_r = c_s I\omega_r/2YI + c_a/2m\omega_r$. Once the damping ratios for two separate vibration modes are known, the two unknown constant damping coefficients c_s and c_a can be mathematically calculated. Yet for non-uniform piezoelectric beam which is partially covered by piezoelectric sheets as in our case, c_s and c_a are no longer constant along the beam length. Whereas, we can still assume that $c_s I(x)$ and $c_a(x)$ are stiffness proportional and mass proportional, respectively, and obtain two constant values of $(c_s I/YI)_{ave}$ and $(c_a/m)_{ave}$. However, to avoid the calculation of these coefficients as well as the inaccuracy caused by the proportional damping assumption, we can obtain ζ_r experimentally using the logarithmic decrement method and proceed to numerical solution of Eq. (14) for the mechanical and electric responses of the GPEH.

Assume the first n^{th} modes are considered. Again, we introduce the state vector:

$$\mathbf{X} = \left\{ \begin{array}{c} X_1 \\ X_2 \\ \vdots \\ X_{2r-1} \\ X_{2r} \\ \vdots \\ X_{2n+1} \end{array} \right\} = \left\{ \begin{array}{c} \eta_1(t) \\ \dot{\eta}_1(t) \\ \vdots \\ \eta_r(t) \\ \dot{\eta}_r(t) \\ \vdots \\ V(t) \end{array} \right\} \qquad (r = 1,2...n) \tag{15}$$

The governing equations can then be written in the state space form as

$$\dot{\mathbf{X}} = \left\{ \begin{array}{c} \dot{\eta}_1(t) \\ \ddot{\eta}_1(t) \\ \vdots \\ \dot{\eta}_r(t) \\ \ddot{\eta}_r(t) \\ \vdots \\ \dot{V}(t) \end{array} \right\} = \left\{ \begin{array}{c} X_2 \\ -2\varsigma_1\omega_1 X_2 - \omega_1^2 X_1 - \chi_1 X_{2n+1} + \phi_1(L) \times \dfrac{\rho_a h l_{tip} U^2}{2}\left[\displaystyle\sum_{i=1,2....} A_i \left(\dfrac{\phi_1(L)X_2}{U} + \phi_1'(L)X_1\right)^i \right] \\ \vdots \\ X_{2r} \\ -2\varsigma_r\omega_r X_{2r} - \omega_r^2 X_{2r-1} - \chi_r X_{2n+1} + \phi_r(L) \times \dfrac{\rho_a h l_{tip} U^2}{2}\left[\displaystyle\sum_{i=1,2....} A_i \left(\dfrac{\phi_r(L)X_{2r}}{U} + \phi_r'(L)X_{2r-1}\right)^i \right] \\ \vdots \\ \dfrac{\displaystyle\sum_{r=1}^{n} \chi_r X_{2r}}{C_P} - \dfrac{X_{2n+1}}{R_L C_P} \end{array} \right\} \tag{16}$$

Like the SDOF model, Eq. (16) can be solved in MATLAB using ode45. Two cases with different numbers of modes employed will be considered in the following model comparison section. Firstly, we only consider the fundamental mode by letting n equal to 1 in Eq.(16), since a GPEH is oscillating near its fundamental frequency [37, 38]. Secondly, in order to get a more accurate expression for the galloping aerodynamic force, we take into account the first three modes (n=3) to investigate how the higher modes influence the overall responses of a GPEH.

4. Model comparison based on experimental validation

4.1. Experimental setup
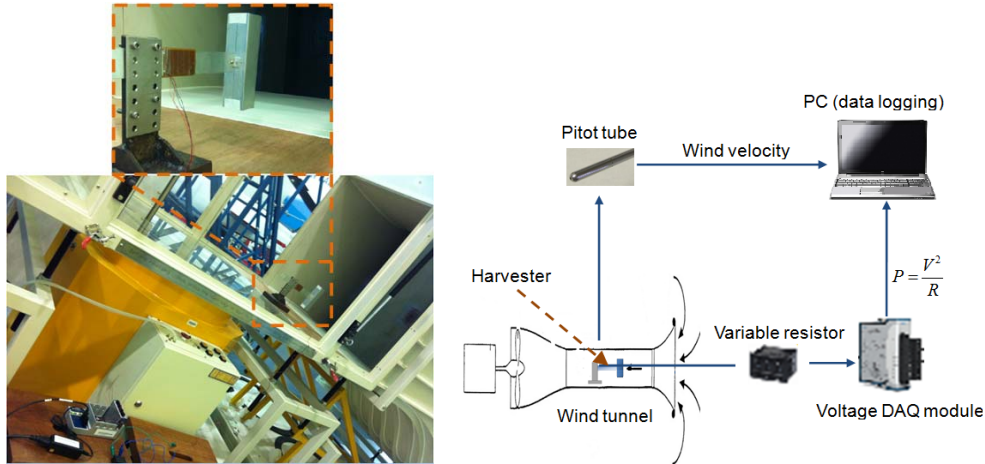
Figure 4. (a) Fabricated prototype and the installation in wind tunnel. (b) Experimental setup

**Table 1.** Parameters of cantilever beam and piezoelectric sheets [36]

Properties	Beam	Piezoelectric sheets	Properties	Beam	Piezoelectric sheets
Length (mm)	150	61	Mass Density (kg m^{-3}）	2700	3825
Width (mm)	30	30	Capacitance (nF)	---	90
Thickness (mm)	0.6	0.5	Young's Modulus (GPa)	69	23.3
Material	Aluminum	DuraAct P-876.A12	Piezoelectric Constant d_{31} (pm V^{-1})	---	-174

Table 2. Parameters of the bluff body for the three configurations

Properties	Configuration 1	Configuration 2	Configuration 3
Cross-section	square	square	square
Section dimensions (mm^2)	40×40	40×40	40×40
Length l_{tip} (mm)	150	150	100
Mass M_{tip} (kg)	0.0268	0.0228	0.0268

A prototype device is fabricated and tested in the wind tunnel following the same experimental setup procedure with the preceding study [36], and the measured results are presented to validate the aforementioned SDOF and distributed parameter models. The effectiveness of the models are compared based on the agreement between their predictions and experiments. The cantilever beam is the same with the one in [36], which is composed of a aluminium substrate with two piezoelectric sheets (DuraAct P-876.A12 from Physik Instrumente) bonded to each side of the root, being connected in parallel with the total capacitance C_p=180nF. A metal support is employed to fix the root of the cantilever in the wind tunnel. A bluff body is attached to the free end. According to the preceding experimental study on the cross-section geometry of the bluff body [36], a square section is employed for its best performance over other geometries in the laminar flow with the lowest cut-in wind speed and the largest output power. Three configurations are tested in the wind tunnel with different bluff body properties for adequate model comparisons. The properties of the beam and piezoelectric sheets are listed in Table 1, while those of the bluff body are shown in Table 2. The prototype and the installation in the wind tunnel are shown in Figure 4(a). Prior to the wind tunnel test, some parameters like ζ, ω_{nsc} and ω_{noc} need to be measured under base excitations. The damping ratio ζ for the SDOF model is the same as ζ_1 in the distributed parameter model. For Configuration 1, ζ_1=0.005[36], ζ_2=0.015 and ζ_3=0.034; for Configuration 2, ζ_1=0.008, ζ_2=0.019 and ζ_3=0.041; for Configuration 3, ζ_1=0.004 ζ_2=0.012, ζ_3=0.031. During the wind tunnel test, the wind speed is measured by a pitot tube anemometer, and the voltage across the load resistance is measured by the NI 9229 DAQ module. Overall experimental setup is presented in Figure 4(b).

4.2. Model comparison
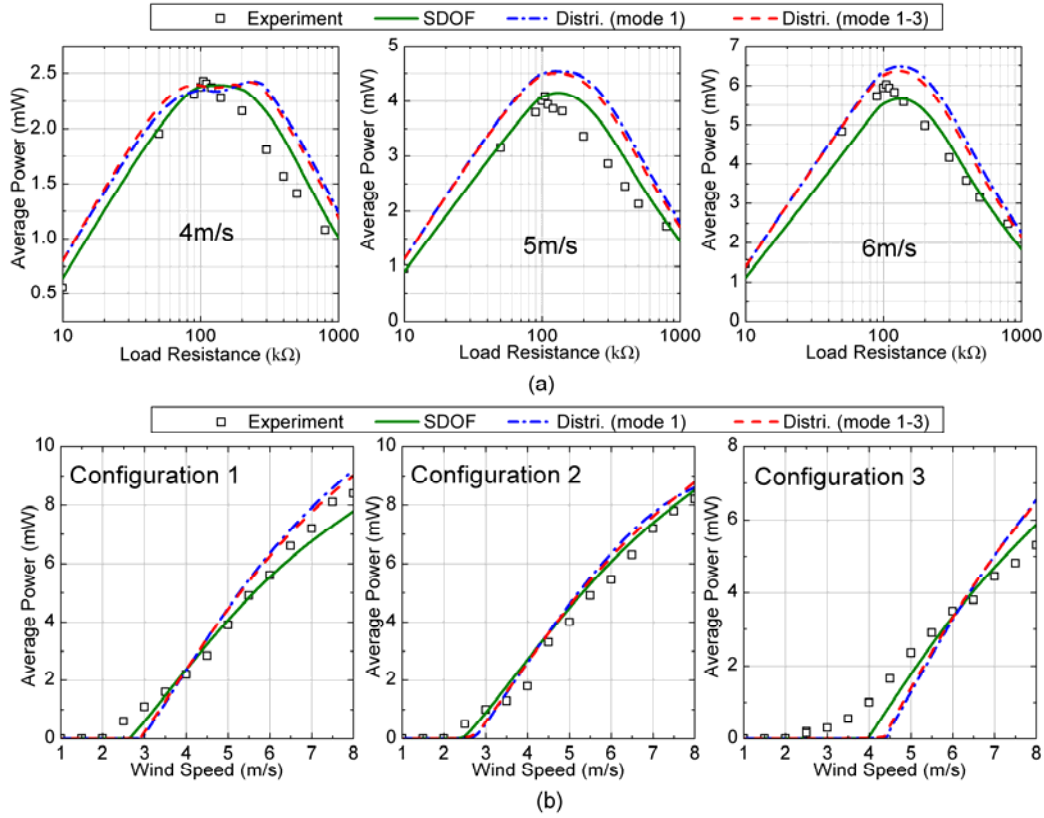
Figure 5. (a) Measured and predicted average power P_{ave} versus load resistance R_L for configuration 1 at $U=4$, 5 *and* 6*m/s*. (b) Measured and predicted average power P_{ave} versus wind speed U for three configurations at the respective optimum R_L.

The measured and predicted values of average power P_{ave} versus load resistance R_L are first compared in Figure 5(a). The data presented are obtained for configuration 1 at three different wind speeds. As shown in the picture, for $U=4$, 5 and 6m/s, P_{ave} initially increases with R_L until reaches an optimum value, then decreases when R_L continues growing. The optimum R_L barely changes for the three wind speeds, which are all around 105~120kΩ. All the three models can capture this trend well, yet with some discrepancies. Also, both the single mode distributed parameter model (shorted for Distri. (mode 1) here and hereafter) and multiple mode distributed parameter model (shorted for Distri. (mode 1-3) here and hereafter) predict a shallow valley around the optimum R_L for $U=4$m/s, which is an important aspect for the influence of R_L on P_{ave} and will be addressed in the next section. Moreover, no obvious difference is observed between the predictions of Distri. (mode 1) and Distri. (mode 1-3). Figure 5(b) shows the measured and predicted P_{ave} versus wind speed U for the three different GPEH configurations at $R_L=105$ kΩ. It is noted that P_{ave} increases monotonically with U. Again, all the three models can predict consistent results with the experiments. As for the cut-in wind speed U_{cr}, the SDOF model predicts better results for all the three configurations, while as for the harvested power level, no obvious superiority is observed for one model over the others since small discrepancies exist for all the three models. The main source of the error is probably the unavoidable small turbulence in the wind tunnel which disturbs the bluff body to start oscillating before the wind speed reaches the real cut-in speed. In general, the

three models can successfully predict the electroaeroelastic behavior with good agreement with the experiments. The SDOF model is advantageous for its simplicity and ease of obtaining the coupling coefficient for a fabricated prototype, while the distributed models own their merits in the better representation of the aerodynamic force and ease for parametric study. In the following study about the effects of different parameters on the output power, Distri. (mode 1) is employed to obtain the simulation results.

5. Parametric study using distributed parameter model (1st mode)
In this section, a parametric study is presented in order to better understand the electroaeroelastic behavior of the GPEH. The effects of load resistance R_L, wind exposure area S_{tip}, mass of the bluff body M_{tip}, and length of the piezoelectric sheets L_p on the cut-in wind speed as well as the output power level are investigated.
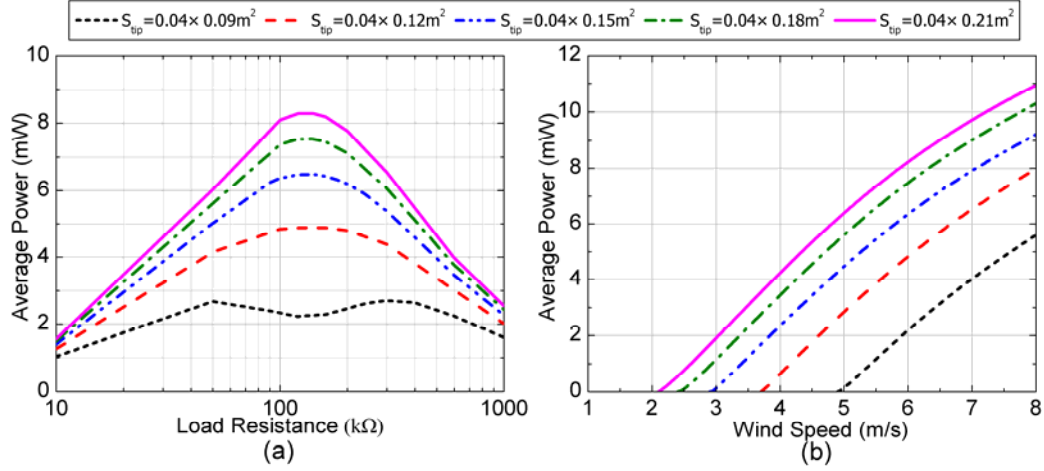
5.1. Effects of the load resistance R_L
Figure 6(a) shows the variation of the average output power P_{ave} with the wind speed U for different load resistance R_L. Here, Configuration 1 is considered and its properties are shown in Table 1 and Table 2. It can be seen that the growth rate of P_{ave} is greatly affected by R_L. The growth rate of P_{ave} firstly increases with R_L until 105kΩ, then decreases when R_L is further increasing. An enlarged view is provided to show this trend more clearly around the threshold of galloping. It is noted that the value of R_L which owns the largest growth rate of P_{ave} also gives the largest cut-in wind speed U_{cr}. The variation of U_{cr} with R_L is presented in Figure 6(b). As can be seen from this curve, U_{cr} increases with R_L up to the maximum value then decreases with R_L. As for the harvested power level, the largest power is obtained with R_L around 105kΩ for U>4m/s. Features of the optimum R_L can be seen from Figure 6(c) which displays the variation of P_{ave} with R_L at different wind speeds. For U=2m/s, P_{ave} is zero between 20 and 800kΩ since this speed is lower than the respective U_{cr} for these R_L values (Figure 6(b)). When U is slightly larger than U_{cr} (i.e., U=3 and 4m/s), a shallow valley exists around 105kΩ. When U continues growing (i.e., U=5~8m/s), there is a peak for P_{ave} between 100 and 120kΩ, where lies the optimum R_L =105kΩ. It is worth mentioning that R_L for the valley and peak of P_{ave} overlap with each other, corresponding to that with the largest U_{cr}. Here onwards, we regard R_L as the optimum one if the largest U_{cr} and power growth rate are achieved in the response of P_{ave} versus U (i.e., the curve for R_L=105kΩ in Figure 6(a)). At the optimum R_L, either a valley or a peak appears in the response of P_{ave} versus R_L at a specific U.
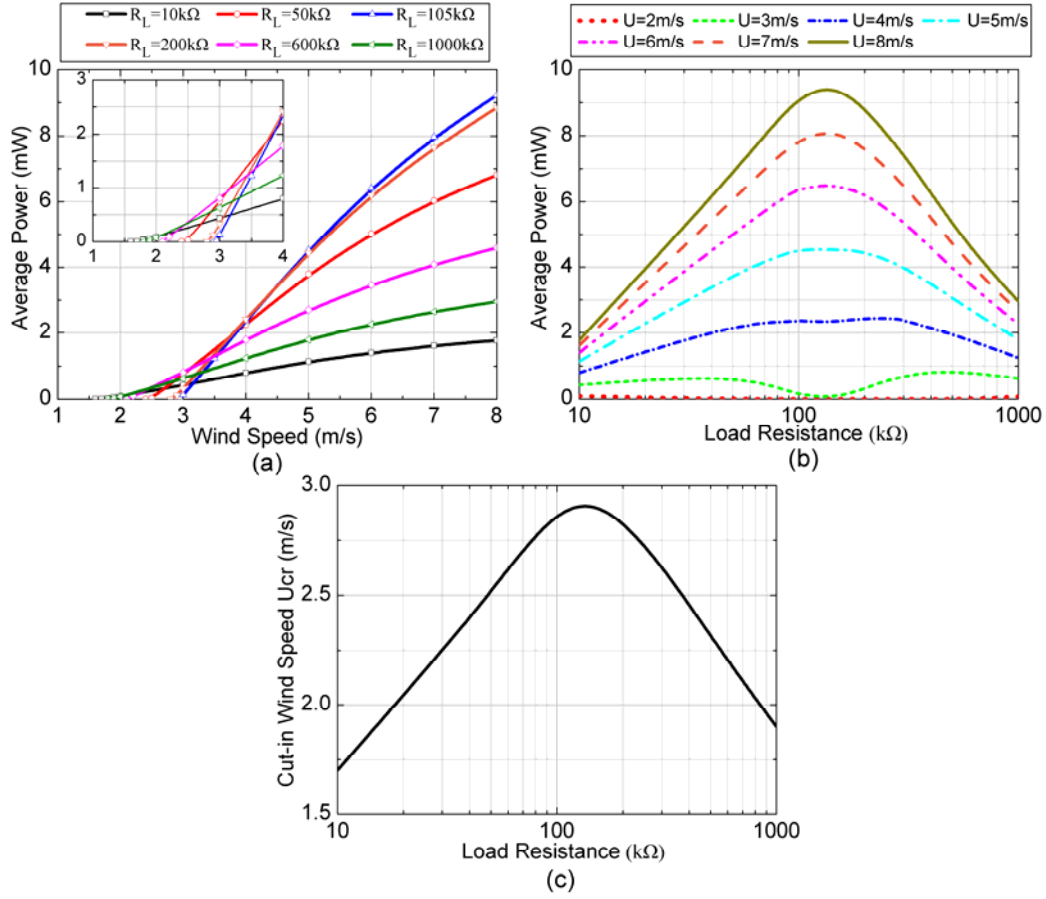
Figure 6. (a) Variation of the average power P_{ave} with the wind speed U for different load resistance. (b) Variation of the average power P_{ave} with the load resistance R_L for different wind speeds. (c) Variation of the cut-in wind speed U_{cr} with the load resistance.

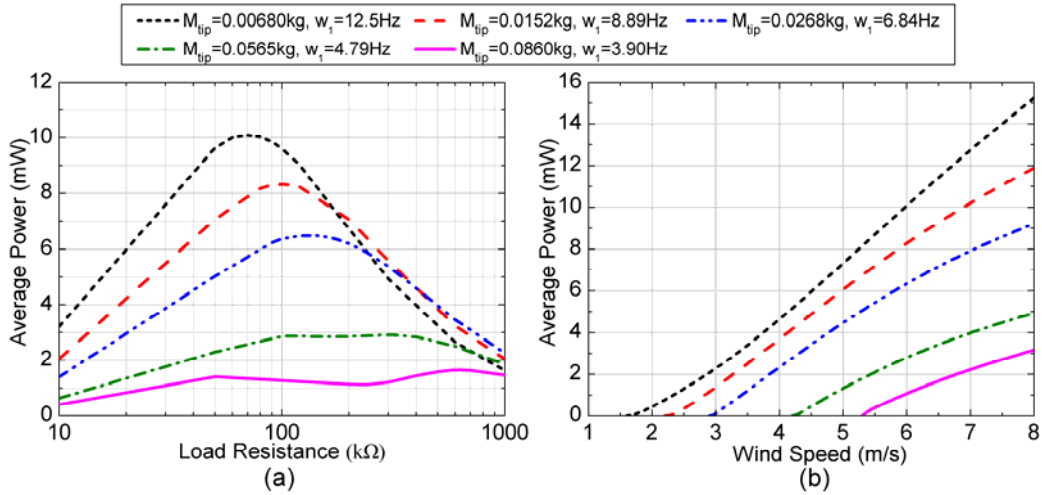### 5.2. Effects of the wind exposure area of the bluff body S_{tip}

Figure 7 shows the effects of the wind exposure area of the bluff body S_{tip} (h×l_{tip}) on the electroaeroelastic behavior of the GPEH. Harvester properties are the same with those listed in Table 1 and Table 2 (Configuration 1) except the length of the bluff body l_{tip}. Figure 7(a) is obtained with U=6m/s. It is determined that the optimum R_L for the various S_{tip} are equal to each other, which is reasonable since the natural frequencies are the same with equal M_{tip}. The variation of P_{ave} with U at the optimum R_L for different S_{tip} is shown in Figure 7(b). With increasing S_{tip}, the cut-in wind speed decreases while the harvested power increases, both beneficial for harvesting the wind power. This can be expected since the increasing wind exposure area results in an increase in the aerodynamic force. Moreover, the growth rate of power is not much affected by S_{tip}.

Figure 7. Variation of (a) the average power P_{ave} with the load resistance R_L at 6m/s and (b) the average power P_{ave} with the wind speed U at the optimum R_L for different wind exposure areas of the bluff body S_{tip}.

5.3. Effects of the mass of the bluff body M_{tip} (or fundamental frequency of the GPEH)

Figure 8 shows the effects of the mass of the bluff body M_{tip} on the electroaeroelastic behavior of the GPEH. Harvester properties are the same with those list in Table 1 and Table 2 (Configuration 1) except M_{tip}. The most obvious change due to varying M_{tip} is in the fundamental frequency of the harvester as indicated in the legend. Figure 8(a) shows the variation of P_{ave} with R_L for U=6m/s, from which the respective optimum R_L can be obtained for each M_{tip}. It is noted that the optimum R_L varies with different M_{tip} (i.e., different fundamental frequency ω_1). With the respective optimum R_L, the variation of P_{ave} with U is displayed in Figure 8(b). As can be seen from this figure, the cut-in wind speed increases and the harvested power decreases with the increasing M_{tip} (or the decreasing of ω_1). Moreover, the growth rate of the harvested power also decreases with the increasing M_{tip}. It can summarized that for the GPEH with a specific piezoelectric cantilever, reducing M_{tip} can achieve a better performance on extracting power from the wind.

*5.4. Effects of the length of the piezoelectric sheets L_p*
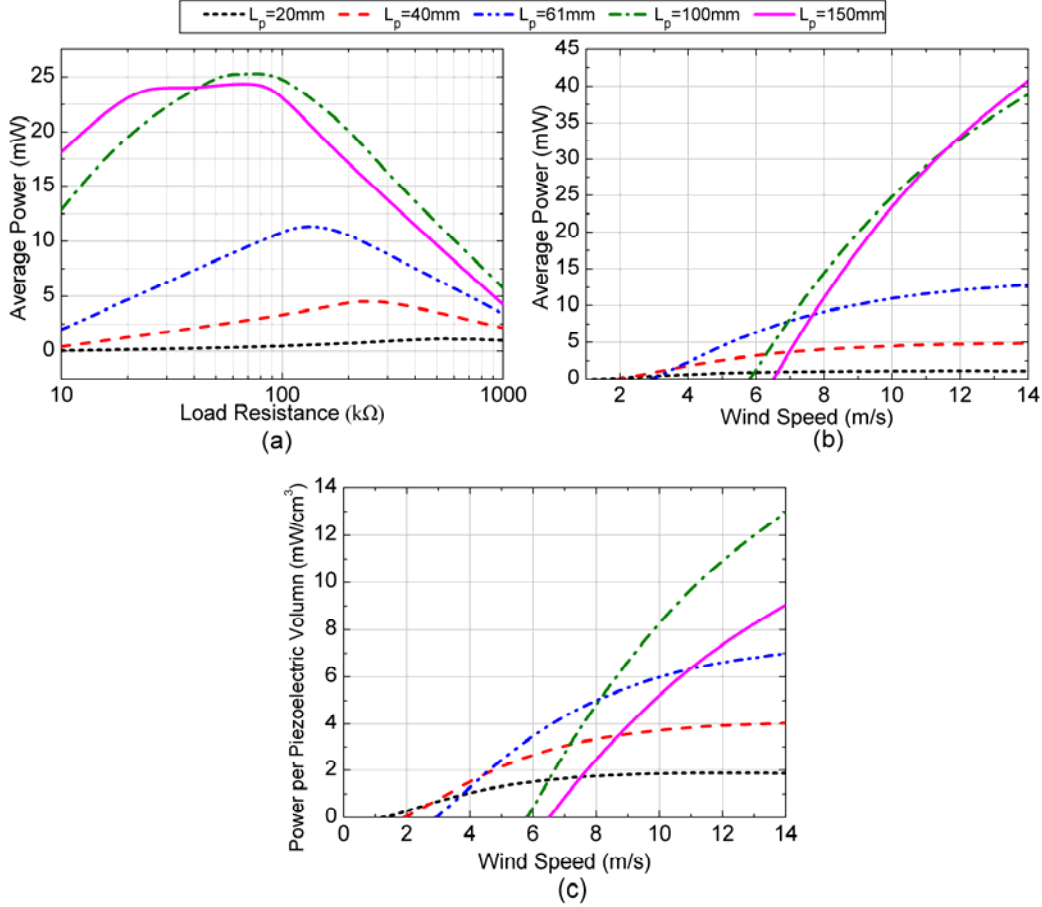
Figure 9. Variation of (a) the average power P_{ave} with the load resistance R_L at 10m/s, (b) the average power P_{ave} with the wind speed U at the respective optimum R_L and (c) the power density with the wind speed U for different lengths of the piezoelectric sheets L_p.

Figure 9 shows the effects of the lengths of piezoelectric sheets L_p on the electroaeroelastic behavior of the GPEH. Harvester properties are the same with those list in Table 1 and Table 2 (Configuration 1) except L_p and C_p since the latter one varies linearly with the former one when other parameters are kept unchanged. The respective optimum R_L is determined from figure 9(a), which varies with L_p because of the change in the total stiffness of the composite beam. Figure 9(b) shows the variation of P_{ave} with U at the respective optimum R_L. The cut-in wind speed as well as the growth rate of the harvested power increases with the increasing L_p. The largest L_p can extract the highest power at relatively high wind speeds (>12m/s). A useful factor to evaluate the performance of the GPEH is the power density which is calculated as power per piezoelectric volume in this paper. Figure 9(c) shows the power density versus the wind speed for different L_p. It is noted that the power density is not monotonically increasing

with L_p. At high wind speeds the highest power density is obtained by a medium value of L_p, which is 100mm among the considered discrete values. A maximum power density of 12.96mW/cm^3 is achieved at 14m/s with L_p=100mm. A comparison of the power density with other piezoelectric wind energy harvesters is shown in Figure 10. As can be seen from this figure, the present GPEH shows good performance in power density, especially at relatively high wind speeds. The present GPEH is less advantageous at lower wind speeds when compared to the harvesters in [15] and [37]. However, the present GPEH owns the largest overall range of wind speed for effective power generation with considerable power density. Note that the data for the present GPEH in the figure is not optimized in the aspects of S_{tip}, M_{tip}, etc.
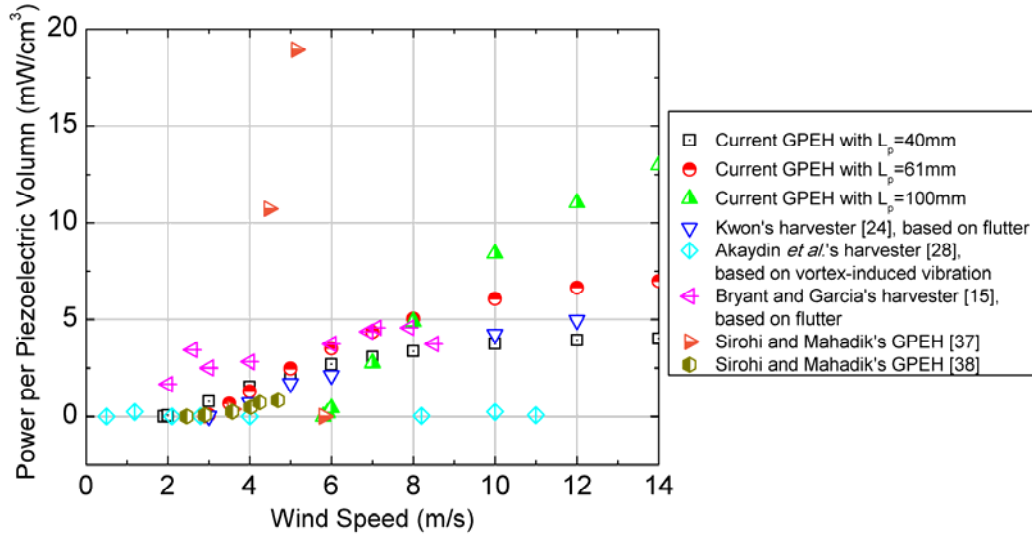
Figure 10. Comparison of the power density with other piezoelectric wind energy harvesters

7. Conclusion

In this paper, a comparison study is presented on the performance of the modelling methods for GPEH, including the SDOF model, single mode and multi-mode Euler-Bernoulli distributed parameter models. A typical GPEH consisting of a piezoelectric cantilever attached to a square-sectioned bluff body is considered. Procedures for these modelling methods are presented, in which the aerodynamic forces are all formulated based on quasi-steady hypothesis. Subsequently, wind tunnel experiments for the fabricated prototypes are conducted to validate and evaluate these models. The results show that all these models can successfully predict the variation of the average power with the load resistance and the wind speed with. Quite small difference is observed between the single-mode and multi-mode Euler-Bernoulli distributed parameter models. The distributed parameter model owns a more rational representation of the aerodynamic force, while the SDOF model gives a better prediction on the cut-in wind speed. In general, the SDOF can predict the electroaeroelastic behavior of a GPEH device accurately enough with its advantage of simplicity and ease of obtaining the electromechanical coupling term.

The influence of the load resistance, wind exposure area and mass of the bluff body, and length of the piezoelectric sheets on the cut-in wind speed as well as the output power level of

the GPEH are investigated with a single-mode Euler-Bernoulli distributed parameter model. It is determined that U_{cr} and the growth rate of P_{ave} increases first with R_L to a certain value, then drops with R_L. When U is large enough the largest P_{ave} is obtained with the optimum R_L, which owns the largest U_{cr} as well. With the corresponding optimum R_L, increasing S_{tip} and decreasing Mtip can increase P_{ave} as well as reduce U_{cr}. For the case of L_p, larger L_p gives larger U_{cr} and larger growth rate of P_{ave}, yet not guarantees larger power density (power per piezoelectric volume), which is obtained at a medium L_p. Compared to other piezoelectric wind energy harvesters, our present GPEH gives higher power density at high wind speeds and owns the largest range of U with considerable power density. Future work involves improving the performance of the GPEH at low wind speeds.

Reference

[1] Roundy S, Wright P K and Rabaey J 2003 A study of low level vibrations as a power source for wireless sensor nodes *Comput. Commun.* **26** 1131–44

[2] El-Hami M, Glynne-Jones P, White N M, Beeby S, James E, Brown A D and Ross J N 2001 Design and fabrication of a new vibration-based electromechanical power generator *Sensors and Actuators* A **92** 335–42

[3] Anton S R and Sodano H A 2007 A review of power harvesting using piezoelectric materials (2003-2006) *Smart Mater. Struct.* **16** R1-R21

[4] Wang L and Yuan F G 2008 Vibration energy harvesting by magnetostrictive material *Smart Mater. Struct.* **17** 045009

[5] Erturk A and Inman D J 2008 A distributed parameter electromechanical model for cantilevered piezoelectric energy harvesters *J. Vib. Acoust.* **130** 041002

[6] Castagnetti D 2012 Experimental modal analysis of fractal-inspired multi-frequency structures for piezoelectric energy converters *Smart Mater. Struct.* **21** 094009

[7] Yang Y, Tang L and Li H 2009 Vibration energy harvesting using macro-fiber composites *Smart Mater. Struct.* **18** 115025.

[8] Tang L, Yang Y and Soh C K 2010 Towards broadband vibration-based energy harvesting *J. Intell. Mater. Syst. Struct.* **21** 1867-97.

[9] Shu Y C and Lien I C 2006 Analysis of power output for piezoelectric energy harvesting systems *Smart Mater. Struct.* **15** 1499-1512

[10] Wickenheiser A M and Garcia E 2010 Power optimization of vibration energy harvesters utilizing passive and active circuits *J. Intell. Mater. Syst. Struct.* **21** 1343-61

[11] Tang L and Yang Y 2011 Analysis of synchronized charge extraction for piezoelectric energy harvesting *Smart Mater. Struct.* **20** 085022

[12] De Marqui C Jr and Erturk A 2012 Electroaeroelastic analysis of airfoil-based wind energy harvesting using piezoelectric transduction and electromagnetic induction *J. Intell. Mater. Syst. Struct.*

[13] Sousa V C, de M Anicézio M, de Marqui C Jr and Erturk A 2011 Enhanced aeroelastic energy harvesting by exploiting combined nonlinearities: theory and experiment *Smart Mater. Struct.* **20** 094077

[14] Boragno C, Festa R and Mazzino A 2012 Elastically bounded flapping wing for energy harvesting *Appl. Phys. Lett.* **25** 253906

[15] Bryant M and Garcia E 2011 Modeling and testing of a novel aeroelastic flutter energy harvester *J. Vib. Acoust.* **133** 011010

[16] Erturk A, Vieira W G R, De Marqui C Jr and Inman D J 2010 On the energy harvesting potential of piezoaeroelastic systems *Appl. Phys. Lett.* **96** 184103

[17] Abdelkefi A, Nayfeh A H and Hajj M R 2012 Enhancement of power harvesting from piezoaeroelastic systems *Nonlinear Dyn.* **68** 531-41

[18] Abdelkefi A, Hajj M R and Nayfeh A H 2012 Sensitivity analysis of piezoaeroelastic energy harvesters *J. Intell. Mater. Syst. Struct.* **23** 1523-31

[19] Bryant M and Garcia E 2009 Development of an aeroelastic vibration power harvester *Proceeding SPIE* **7288** 728812

[20] Abdelkefi A, Nayfeh A H and Hajj M R 2012 Modeling and analysis of piezoaeroelastic energy harvesters *Nonlinear Dynamics* **67** 925-939

[21] Abdelkefi A, Nayfeh A H and Hajj M R 2012 Design of piezoaeroelastic energy harvesters *Nonlinear Dynamics* **68** 519-530

[22] Doare O and Michelin S 2011 Piezoelectric coupling in energy harvesting fluttering flexible plates: linear stability analysis and conversion efficiency *Journal of Fluids and Structures* **27** 1357-1375

[23] Li S, Yuan J and Lipson H 2011 Ambient wind energy harvesting using cross-flow fluttering *J. Appl. Phys.* **109** 026104

[24] Kwon S D 2010 A T-shaped piezoelectric cantilever for fluid energy harvesting *Appl. Phys. Lett.* **97** 164102

[25] Weinstein L A, Cacan M R, So P M and Wright P K 2012 Vortex shedding induced energy harvesting from piezoelectric materials in heating, ventilation and air conditioning flows *Smart Mater. Struct.* **21** 045003

[26] Barrero-Gil A, Pindado S and Avila S 2011 Extracting energy from vortex-induced vibrations: a parametric study *Appl. Math. Model.* **36** 3153-60

[27] Sivadas V and Wickenheiser A M 2011 A study of several vortex-induced vibration techniques for piezoelectric wind energy harvesting *Proc. SPIE – Int. Soc. Opt. Eng.* vol **7977** p 79770F

[28] Akaydin H D, Elvin N and Andreopoulos Y 2012 The performance of a self-excited fluidic energy harvester *Smart Mater. Struct.* **21** 025007

[29] Abdelkefi A, Hajj M R and Nayfeh A H 2012 Phenomena and modeling of piezoelectric energy harvesting from freely oscillating cylinders *Nonlinear Dynamics* **70** 1355–1363

[30] Jung H J and Lee S W 2011 The experimental validation of a new energy harvesting system based on the wake galloping phenomenon *Smart Mater. Struct.* **20** 055022

[31] Elvin N G and Elvin A A 2009 The flutter response of a piezoelectrically damped cantilever pipe *J. Intell. Mater. Syst. Struct.* **20** 2017-26

[32] Bibo A, Li G and Daqaq M F 2012 Performance analysis of a harmonica-type aeroelastic micropower generator *J. Intell. Mater. Syst. Struct.* **23** 1461-74

[33] Barrero-Gil A, Alonso G and Sanz-Andres A 2010 Energy harvesting from transverse galloping *J. Sound Vib.* **329** 2873-83

[34] Abdelkefi A, Hajj M R and Nayfeh A H 2012 Power harvesting from transverse galloping of square cylinder *Nonlinear Dynamics* **70** 1377-88

[35] Abdelkefi A, Hajj M R and Nayfeh A H 2013 Piezoelectric energy harvesting from transverse galloping of bluff bodies *Smart Mater. Struct.* **22** 015014

[36] Yang Y, Zhao L and Tang L 2013 Comparative study of tip cross-sections for efficient galloping energy harvesting *Appl. Phys. Lett.* **102**(6) 064105

[37] Sirohi J and Mahadik R 2011 Piezoelectric wind energy harvester for low-power sensors *J. Intell. Mater. Syst. Struct.* **22** 2215-28

[38] Sirohi J and Mahadik R 2012 Harvesting wind energy using a galloping piezoelectric beam *J. Vib. Acoust.* **134** 011009

[39] Abdelkefi A, Yan Z and Hajj M R 2013 Modeling and nonlinear analysis of piezoelectric energy harvesting from transverse galloping *Smart Mater. Struct.* **22** 025016

[40] Den Hartog J P 1956 *Mechanical Vibrations* (New York: McGraw-Hill)

[41] Barrero-Gil A, Sanz-Andrés A and Roura M 2009 Transverse galloping at low Reynolds numbers *J. Fluids Struc.* **25** 1236-42

[42] Alonso G, Meseguer J and Perez-Grande I 2007 Galloping stability of triangular cross-sectional bodies: a systematic approach *J. Wind Eng. Ind. Aerodyn.* **95** 928-40

[43] Alonso G and Meseguer J 2006 A parametric study of the galloping stability of two-dimensional triangular cross-section bodies *J. Wind Eng. Ind. Aerodyn.* **94** 241-53

[44] Luo S C, Chew Y T, Lee T S and Yazdani M G 1998 Stability to translational galloping vibration of cylinders at different mean angles of attack *J. Sound Vib.* **215** 1183-94

[45] Païdoussis M P, Price S J and De Langre E 2011 *Fluid-Structure Interactions: Cross-Flow-Induced Instabilities* (New York: Cambridge University Press)

[46] Erturk A and Inman D J 2008 On mechanical modeling of cantilevered piezoelectric vibration energy harvesters *J. Intell. Mater. Syst. Struct.* **19** 1311-25

[47] Erturk A and Inman D J 2008 Issues in mathematical modeling of piezoelectric energy harvesters *Smart Mater. Struct.* **17** 065016